

REPORT DOCUMENTATION PAGE

Form Approved
OMB No. 0704-0188

Public reporting burden for this collection of information is estimated to average 1 hour per response, including the time for reviewing instructions, searching existing data sources, gathering and maintaining the data needed, and completing and reviewing this collection of information. Send comments regarding this burden estimate or any other aspect of this collection of information, including suggestions for reducing this burden to Department of Defense, Washington Headquarters Services, Directorate for Information Operations and Reports (0704-0188), 1215 Jefferson Davis Highway, Suite 1204, Arlington, VA 22202-4302. Respondents should be aware that notwithstanding any other provision of law, no person shall be subject to any penalty for failing to comply with a collection of information if it does not display a currently valid OMB control number. PLEASE DO NOT RETURN YOUR FORM TO THE ABOVE ADDRESS.

1. REPORT DATE (DD-MM-YYYY)

2. REPORT TYPE

Technical Papers

3. DATES COVERED (From - To)

4. TITLE AND SUBTITLE

5a. CONTRACT NUMBER

5b. GRANT NUMBER

5c. PROGRAM ELEMENT NUMBER

6. AUTHOR(S)

5d. PROJECT NUMBER

1011

5e. TASK NUMBER

CA9F

5f. WORK UNIT NUMBER

7. PERFORMING ORGANIZATION NAME(S) AND ADDRESS(ES)

Air Force Research Laboratory (AFMC)
AFRL/PRS
5 Pollux Drive
Edwards AFB CA 93524-7048

8. PERFORMING ORGANIZATION
REPORT

9. SPONSORING / MONITORING AGENCY NAME(S) AND ADDRESS(ES)

Air Force Research Laboratory (AFMC)
AFRL/PRS
5 Pollux Drive
Edwards AFB CA 93524-7048

10. SPONSOR/MONITOR'S
ACRONYM(S)

11. SPONSOR/MONITOR'S
NUMBER(S)

12. DISTRIBUTION / AVAILABILITY STATEMENT

Approved for public release; distribution unlimited.

13. SUPPLEMENTARY NOTES

14. ABSTRACT

20030110 123

15. SUBJECT TERMS

16. SECURITY CLASSIFICATION OF:

17. LIMITATION
OF ABSTRACT

18. NUMBER
OF PAGES

19a. NAME OF RESPONSIBLE
PERSON

Leilani Richardson

19b. TELEPHONE NUMBER

(include area code)
(661) 275-5015

a. REPORT

b. ABSTRACT

c. THIS PAGE

Unclassified

Unclassified

Unclassified

A

Standard Form 298 (Rev. 8-98)
Prescribed by ANSI Std. Z39.18

18 separate items enclosed

1011-2-8
TP-1998-075

MEMORANDUM FOR IN-HOUSE PUBLICATIONS

FROM: PROI (TI) (STINFO)

22 Apr 98

SUBJECT: Authorization for Release of Technical Information, Control Number: AFRL-PR-ED-TP-1998-075
Timothy C. Miller "Mode Mixity Determinations for Interfacial Cracking in Incompressible Materials
Under Plane Strain Conditions"
(Statement A)

Mode Mixity Determinations for Interfacial Cracking in Incompressible Materials under Plane Strain Conditions

T. C. Miller

Sparta, Inc., 4 Draco Drive, Edwards Air Force Base, California 93524

Introduction

A frequent site for the development of cracks is along the interface between two materials, for example, the interface between the rubber liner and the propellant grain in a solid rocket motor. Cracks along this interface experience plane strain conditions and are bounded by two incompressible materials. These conditions lead to a simplified analysis so that complete determination of the complex stress intensity factor is straightforward [1,2]. To study plane strain interfacial cracking in incompressible material pairs, researchers used the photoelastic stress freezing method. Transparent materials which exhibit changes in the index of refraction when stressed are loaded at a temperature above a temperature T_c , known as the stress freezing temperature. Lowering the temperature below T_c while maintaining the load "locks in" the stress data through local variations in the index of refraction. Illumination with laser light reveals fringe patterns; these fringes are proportional to the maximum in-plane shear stress. Subsequent slicing of the specimen does not affect the fringe patterns and allows for analysis of the stresses in three dimensions [1].

To analyze plane strain incompressible interfacial fracture, specimens were constructed from two materials. The first was a plastic, araldite, and the second was the same plastic with the addition of aluminum particles. Young's moduli for these two materials were 18.6 and 36.9 MPa, respectively, for the araldite and the araldite-aluminum, so that the two moduli differed by a factor of about two (in solid rocket motors, the mismatch of the two moduli is between two and three). Different mode mixities were introduced by varying the crack orientation in different specimens while keeping the loading direction constant. Crack orientations of $\Gamma = 0^\circ$, 15° , 30° , and 45° were considered, where $\Gamma = 0^\circ$ corresponds to mode I loading (see Fig. 1). Analysis of the photoelastic fringe pattern provided results for the magnitude and phase angle of the complex stress intensity factor for a range of mode mixities [1].

Figure 1 shows one of the finite element meshes used to model these specimens. The mesh used eight noded plane strain quadrilateral elements. Elements around the crack tip are quadrilaterals degenerated into triangular elements with quarter point nodes. All of the singularity elements have the same node at the crack tip. The notch geometry shown matches that used in the photoelastic experiment. Boundary conditions are applied using point loads at the top of the aluminum grips (to which the specimens were glued) which were allowed to rotate freely (as were the actual grips used in the experiment). In the experiment, an adhesive was used to bond the two materials together. The modulus of the adhesive was similar to that of the araldite-aluminum (they differed by 12%), and the adhesive layer was thin (less than 0.5 mm). Because the layer was thin and its properties were similar to one of the other materials, the adhesive layer did not affect the fracture parameters, and was not incorporated into the finite element models.

DISTRIBUTION STATEMENT A
Approved for Public Release
Distribution Unlimited

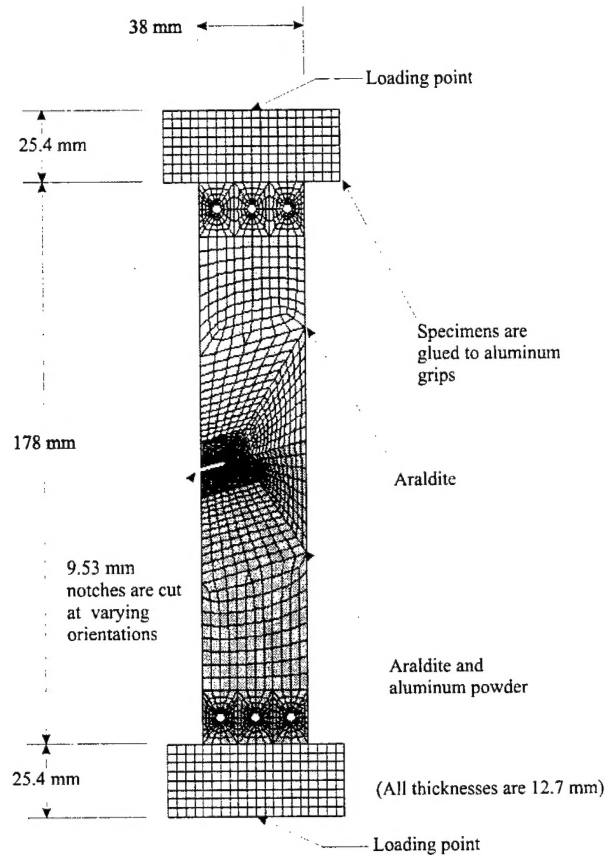


Figure 1 - Typical Finite Element Mesh Used in Numerical Computations (crack orientation = 15 degrees).

Mixed Formulations and Incompressibility

Plane strain conditions in incompressible materials require special solution techniques; in particular, a mixed mode formulation must be used. The constitutive model for an isotropic linear elastic material can be expressed as:

$$\sigma_{ij} = K \epsilon_v \delta_{ij} + 2\mu \epsilon'_{ij}$$

$$\mu = \frac{E}{2(1 + \nu)} \quad K = \frac{E}{3(1 - 2\nu)} \quad (1)$$

$$\epsilon_v = \epsilon_{kk} \quad \epsilon'_{ij} = \epsilon_{ij} - \frac{1}{3} \epsilon_v \delta_{ij}$$

Here σ_{ij} is the stress tensor, ϵ_{ij} is the strain tensor, ϵ'_{ij} is the deviatoric strain tensor, and ϵ_v is the volumetric strain component. The bulk modulus and shear modulus, K and μ , characterize the resistance of the material to compression (or expansion) and shear deformations. However, as Poisson's ratio, ν , approaches $\frac{1}{2}$, the bulk modulus becomes infinite and the volumetric strain approaches zero. This makes the constitutive form of eq. (1) indeterminate, so that the stresses require an additional variable (such as pressure or hydrostatic stress)

for their characterization [3-5]:

$$\sigma_{ij} = -p\delta_{ij} + 2\mu\epsilon'_{ij}, \quad p = -K\epsilon_v. \quad (2)$$

When attempting to model an incompressible material using the finite element method, as $\nu \rightarrow 1/2$, the diagonal terms of the local stiffness matrices approach zero, resulting in an ill-conditioned global stiffness matrix. This ill-conditioning leads to poor predictions of stress if a conventional (i.e., displacement based) finite element formulation is used. The remedy is to use a mixed formulation, where the pressure is a solution variable as well as the displacement components. The problem is then solved by minimizing the total potential energy, which now incorporates the additional constraint $p = -K\epsilon_v$ as a Lagrange multiplier term. Minimizing this revised potential energy expression is realized in the finite element analysis as a mixed mode solution incorporating hybrid elements [3]. The solution variables for each element are the two components of displacement at each node and three pressure terms (which allow for linear pressure variations within each element) [4,5].

Determination of Fracture Parameters

The general solution for a crack along an interface between two isotropic linear elastic materials consists of terms related to an infinite series of complex eigenvalues [6]. In a region near the crack tip, the first eigenvalue term dominates, so that without mode III loading the asymptotic field equations are given by [7]:

$$\sigma_{pq} = \frac{1}{\sqrt{2\pi r}} \{ \text{Re}(\mathbf{K}r^{i\epsilon}) \Sigma_{pq}^I(\theta) + \text{Im}(\mathbf{K}r^{i\epsilon}) \Sigma_{pq}^{II}(\theta) \}. \quad (3)$$

Here $\Sigma_{pq}^I(\theta)$ and $\Sigma_{pq}^{II}(\theta)$ are dimensionless mode I and mode II angular functions and \mathbf{K} is the complex stress intensity factor, which is commonly characterized either by its real and imaginary parts or in a polar form ($\mathbf{K} = K_1 + iK_2 = Ke^{i\psi}$).¹ The coordinate system is at the crack tip, with the x axis parallel to the interface. The two modes of loading are coupled in that their proportions vary with distance from the crack tip for any given set of ~~the~~ applied loads. The bimaterial parameter ϵ is really the complex part of the asymptotic eigenvalue $\lambda = 1/2 + i\epsilon$, and is related to the second Dundurs parameter, β [2]:

$$\epsilon = \frac{1}{2\pi} \text{Ln}\left(\frac{1 - \beta}{1 + \beta}\right), \quad \beta = \frac{\mu_1(\kappa_2 - 1) - \mu_2(\kappa_1 - 1)}{\mu_1(\kappa_2 + 1) + \mu_2(\kappa_1 + 1)}. \quad (4)$$

Here μ is the shear modulus, $\kappa = 3 - 4\nu$ (in plane strain), and the subscripts index the two materials. The presence of the complex part of the eigenvalue causes the inherent mode coupling and leads to other complications such as predicting crack face interpenetration. However, substituting $\nu = 1/2$ and $\kappa = 3 - 4\nu$ in the equations above gives $\epsilon = \beta = 0$, so that for incompressible materials and plane strain conditions, these complications vanish. Similar expressions can be written that use ~~of~~ the complex variables representation. In particular, along the bonded portion of the interface [8]:

¹Throughout the text, \mathbf{K} denotes the complex stress intensity factor, and K denotes its magnitude.

$$(\sigma_{yy} + i\sigma_{xy})_{\theta=0} = \frac{K}{\sqrt{2\pi r}} = \frac{K_1 + iK_2}{\sqrt{2\pi r}} \quad (5)$$

This equation shows that $\tan^{-1}[K_2/K_1]$ and $\tan^{-1}[(\sigma_{xy}/\sigma_{yy})_{\theta=0}]$ are equal in the asymptotic region. The finite element data near the crack tip can be used to determine $\tan^{-1}[K_2/K_1]$ easily, or the phase angle of K , by extrapolating to $r = 0$. To implement this algorithm, stress components σ_{xy} and σ_{yy} are averaged at the nodes along the bond line, then their arctangent is plotted versus r (normalized by the crack length, a) in a certain region near the crack tip. In this work, the first four points near the crack tip were excluded due to difficulties with adequately modeling the high gradients very near the crack tip. Also, points with $r/a \geq 1$ were excluded; far from the crack the stresses approximate those of a plate subjected to combined tension and shear loading or approach a traction free surface condition (as the free surface is approached). The remaining data is fit with a cubic polynomial, and the limit is taken as $r \rightarrow 0$, so that the constant term in the polynomial is an estimate of Ψ :

$$\Psi = \lim(r \rightarrow 0) [(\sigma_{xy}/\sigma_{yy})_{\theta=0}] \approx \lim(r/a \rightarrow 0) \psi(r/a) \quad (6)$$

Here Ψ is the complex stress intensity factor phase angle and ψ is the fitting function for $\tan^{-1}[(\sigma_{xy}/\sigma_{yy})_{\theta=0}]$. In practice both the fitting function and its domain can be arbitrarily chosen provided that they adequately represent the data near the crack tip.

Magnitudes can also be determined easily when $\epsilon = 0$. The magnitude of K is related to the energy release rate [8]:

$$J = G = \frac{K^2}{E^*}, \quad \frac{1}{E^*} = \frac{1}{2} \left[\frac{1}{E_1} + \frac{1}{E_2} \right], \quad \bar{E}_1 = \frac{E_1}{1 - \nu_1^2}, \quad \bar{E}_2 = \frac{E_2}{1 - \nu_2^2} \quad (7)$$

The J integral can be easily calculated using techniques such as virtual crack extension or the domain integral method, and K can then be determined. Finite element data can be used to characterize the complex stress intensity factor completely by (a) simple curve fitting and extrapolation of bond line traction data to determine the phase angle and (b) deriving the magnitude from J values and the effective plane strain modulus, E^* .

Results

Figure 2 shows σ_{yy} contour plots for each of the four geometries considered (in these plots, each specimen has been subjected to a remotely applied tensile stress of 9.65 kPa). The mode mixity for the crack increases approximately linearly with the crack orientation angle Γ , so that the contour plots show the variance of σ_{yy} with mode mixity. A comparison of the four contour plots shows that the size of the σ_{yy} contours decreases as the loading changes from mode I to mode II. Figure 3 shows the commensurate increase in the size of the σ_{xy} contours. The invariance in the shapes of the contours shown in these two figures suggests that the asymmetries shown here are caused by the mismatch of the two elastic moduli rather than changes in the mode mixity. This shows that experimental methods that use fringes proportional to either σ_{yy} or σ_{xy} cannot be used to determine the mode mixity. The shape of the maximum in-plane shear stress contours depends strongly on the mode mixity,

so that experimental methods that exploit this (such as the photoelastic stress freezing method) can be used for mode mixity determination.

For the contour plots shown, the applied stresses were all identical, but in the photoelastic experiment the loads ~~were~~ varied. Experimental results presented here are for slices taken from the mid-thickness of the specimens, so that plane strain conditions were being measured (the finite element models use plane strain elements to model these slices). Table 1 gives a comparison of the experimental and computational results. Residual and machining stresses induced during specimen fabrication caused the high experimental stress intensity magnitudes shown for the $\Gamma = 0^\circ$ and 15° specimens. These stresses cause "no load" fringes that lie parallel to the bond line. When $\Gamma = 0^\circ$, these residual stress fringes affect the gradient of the fringes in the y direction, which is used to calculate K, but this effect diminishes as the crack orientation angle increases. The finite element model assumes an initial state free from these residual stresses, so that the computational calculations for K are perhaps more accurate than the experimental results for the lower values of Γ . However, additional experimental testing can be used to adjust for the effects of residual and machining stresses if necessary. Table 1 also shows the phase angle comparisons. The computational and experimental results agree within 5° for each specimen tested. This suggests that the finite element models can be used to characterize K for other similar geometries, such as those found in solid rocket motors.

crack orientation [deg]	nominal stress [kPa]	magnitudes [kPa m ^{1/2}]		phase angles [deg.]	
		computational	experimental	computational	experimental
0	60.3	15.8	19.0	4.0	0.0
15	96.5	24.0	30.2	11.5	7.8
30	96.5	20.8	20.3	19.5	17.1
45	48.3	7.2	8.3	25.8	30.0

Conclusions

When a crack experiences plane strain conditions and lies along the interface between incompressible materials, the near tip field equations are simplified by the vanishing of the bimaterial parameter, ϵ . Finite element models that use a mixed formulation can be used to characterize the complex stress intensity factor of these cracks completely. This is done by using J integral calculations and a regression of the ratio of bond line traction components to $r = 0$.

References

1. Smith, C. W., Finlayson, E. F., and Liu, C. T. (1997), "A Method for Evaluating Stress Intensity Distribution for Cracks in Rocket Motor Bondlines," Engineering Fracture Mechanics, Vol. 58, pp. 97-105.
2. Dally, J. W. and Riley, W. F. (1991), Experimental Stress Analysis (3rd edition), McGraw Hill.
3. Bathe, K. J. (1996), Finite Element Procedures, Prentice-Hall.
4. ABAQUS/Standard User's Manual, Version 5.5 (1995), Vol. 1, Hibbitt, Karlsson, and Sorenson.
5. ABAQUS Theory Manual, Version 5.5 (1995), Vol. 1, Hibbitt, Karlsson, and Sorenson.
6. Williams, M. L. (1959), "The Stress Around a Fault or Crack in Dissimilar Media," Bulletin of the

Seismological Society of America, Vol. 49, pp. 199-204.

7. Rice, J. R., Suo, Z., and Wang, J. S. (1990), "Mechanics and Thermodynamics of Interfacial Failure in Bimaterial Systems," Metal-Ceramic Interfaces, Ed. M. Ruhle, A. G. Evans, M. F. Ashby, and J. P. Hirth, Pergamon Press.

8. Rice, J. R. (1988), "Elastic Fracture Mechanics Concepts for Interfacial Cracks," Journal of Applied Mechanics, Vol. 55, pp. 98-103.

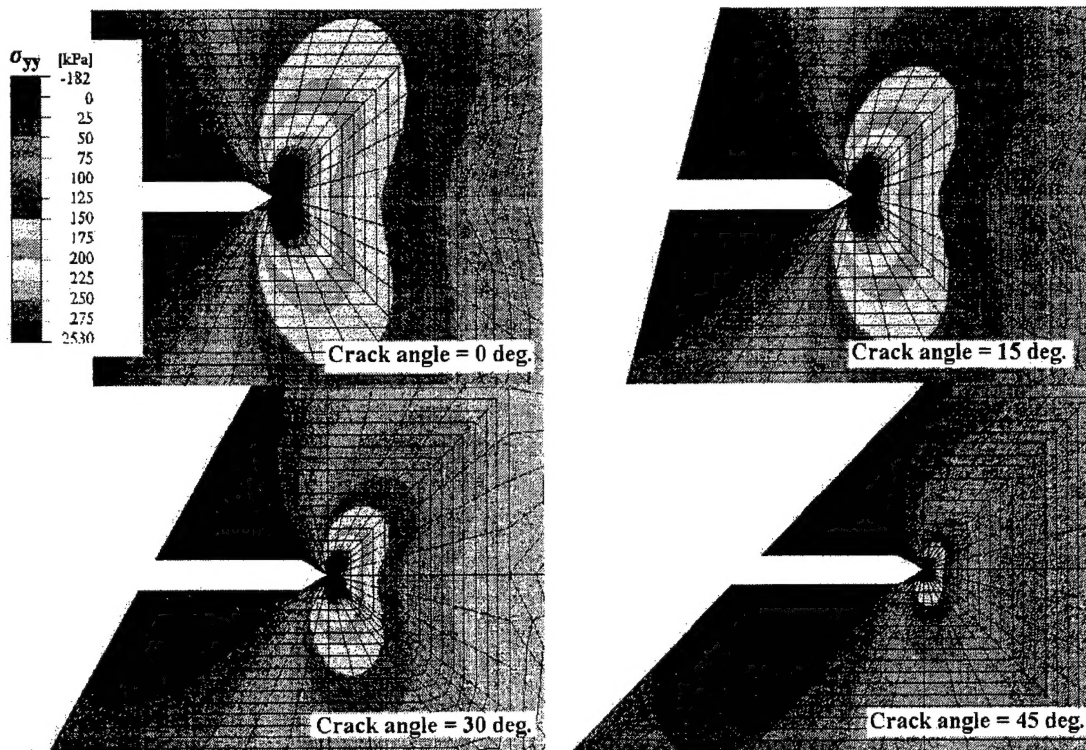


Figure 3 - Contour Plots of Normal Stress for Different Mode Mixities

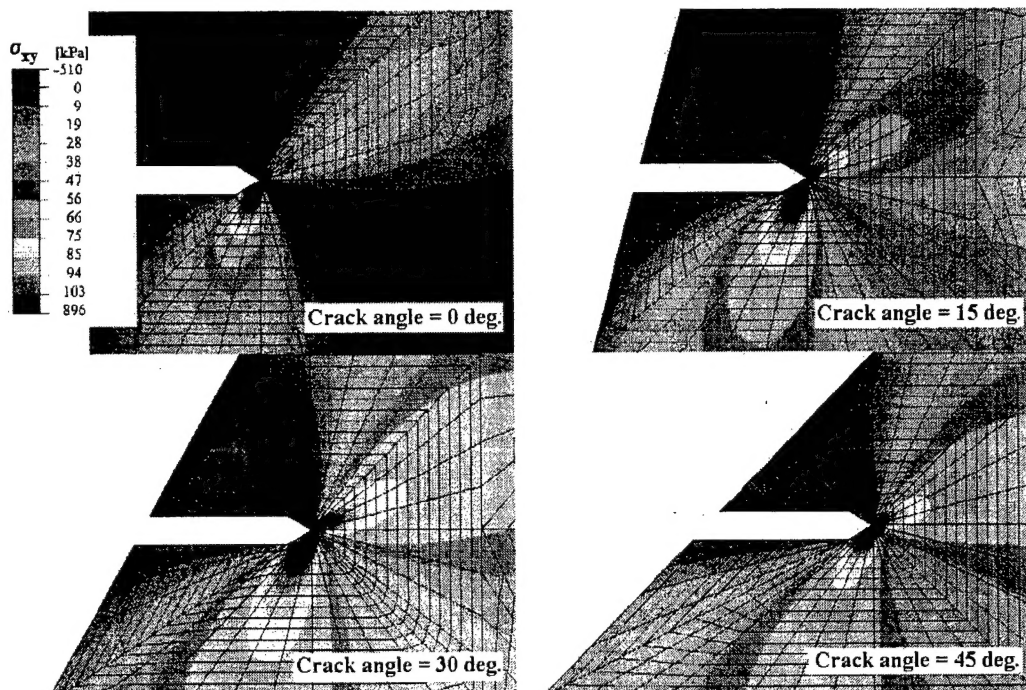


Figure 2 - Contour Plot of Stresses for Different Mode Mixities